Maximal coin-position entanglement and non-Hermitian skin effect in discrete-time quantum walks

Ding Cheng,[1] Yi Li,[2] Hao Zhao,[1, *] Haijun Kang,[3] Cui Kong,[1]
Jiguo Wang,[1] Feng Mei,[2, 4] Chuanjia Shan,[1] and Jibing Liu[1]

[1]*College of Physics and Electronic Science, Hubei Normal University, Huangshi 435002, China*
[2]*State Key Laboratory of Quantum Optics Technologies and Devices,*
Institute of Laser Spectroscopy, Shanxi University, Taiyuan, Shanxi 030006, China
[3]*Science School, Qingdao University of Technology, Qingdao 266520, China*
[4]*Collaborative Innovation Center of Extreme Optics,*
Shanxi University, Taiyuan, Shanxi 030006, China

A distinctive feature of non-Hermitian systems is the skin effect, which has attracted widespread attention in recent studies. Quantum walks provide a powerful platform for exploring the underlying mechanisms of the non-Hermitian skin effect. Additionally, the generation of hybrid entanglement in quantum walks is recognized as another crucial property. However, the experimentally exploring the influence of skin effect on the evolution of entanglement dynamical in the non-Hermitian system remains a challenge. In this paper, we present a flexible photonic implementation of discrete-time quantum walks over 20 evolution steps using an optimized time-multiplexed loop configuration. Through optimizing the coin parameter, we achieve maximal coin-position entanglement in 20-steps quantum walks. Moreover, we experimentally measure the polarization-averaged growth rates and the evolution of coin-position entanglement for specific coin and loss parameters. We observe the asymmetric Lyapunov exponent profiles and the suppression of entanglement induced by the skin effect in non-Hermitian systems. Interestingly, this entanglement suppression weakens with increasing coin parameters and enhances with increasing loss parameters and evolution steps. Our results demonstrate the potential of quantum walks as a powerful platform for investigating hybrid entanglement properties and skin effect in non-Hermitian systems.

I. INTRODUCTION

Quantum walks (QWs) extend classical random walks processes into the quantum realm through coherent superposition of position states. In QWs, the quantum walker's wavefunction maintains coherent delocalization across lattice sites via the unitary evolution, enabling interference between multiple propagation paths. Such transport mechanisms generate ballistic spreading characteristics and lead to a faster spread of the walkers' positions compared to the classical case[1, 2]. The unique space-time evolution has significant advantages in the general-purpose quantum computers[3, 4], quantum simulators[5, 6], and search algorithms[7–9].

For the discrete-time QWs (DTQWs), this generally refer to the coin-based quantum walk[10], namely flipping a coin and moving in the direction determined by the result of the coin flip. The walker's coin and position degrees of freedom can be entangled with each other[11, 12]. The entanglement here is different from its original definition between multiple parties, which is defined between different degrees of freedom of the particles and called hybrid coin-position entanglement[13, 14]. The entanglement fluctuates at each step, gradually stabilizing to an asymptotic value. This stabilization depends on factors such as the coin operation, the shift operation, the initial state, and on-site loss. The re-

sulting entanglement is typically not a maximally entangled state. Thus, generation of the maximal coin-position entanglement and its related research have attracted widespread attention[13–17]. Moreover, DTQWs also provide a platform for studying the fundamental mechanisms of non-Hermitian physics, including exception points[18], topological phase transition[19–21] and non-Hermitian skin effects (NHSE)[21–23]. The NHSE refers to the phenomenon in which bulk eigenstates of a non-Hermitian system become exponentially localized at the its boundaries. In the DTQWs, the on-site loss refers to polarization-dependent loss, which introduces an asymmetric hopping amplitude as a source of non-Hermiticity[23, 24]. The interplay of the on-site polarization-dependent loss and the effective coupling between the coin and position states can experimentally realize NHSE. This effect has led to exciting applications, including funneling of light[25], the topological sensors[26], and topological amplification[27]. Furthermore, non-Hermitian theories offer profound understanding into the dynamics of quantum correlations and entanglement among particles in open quantum systems[27, 28]. The suppression of entanglement and reduction of von Neumann entropy induced by NHSE has been explored with theoretical studies in open condensed matter[24] and experimentally confirmed in the non-Hermitian photonic lattices system with a short evolution period[29]. However, experimental studies to investigate the effect of NHSE on the evolution of entanglement dynamics in non-Hermitian systems are yet challenging.

To date, DTQWs have been taken in a variety of physical systems, including superconducting qubits[30, 31], nuclear magnetic resonance[32], trapped atoms [33], trapped ions[34, 35], integrated photonic circuits[36, 37], or optics system[13–15, 18–23, 38–45]. Photons are an excellent carrier of quantum state due to their low transmission loss in both free space and optical fiber channels. Therefore, optical systems have made remarkable progress in realizing DTQWs with a variety of well-established technologies, including orbital angular momentum (OAM) [38, 39], time multiplexing [13–15, 23, 40–43], and spatial displacers [18–22, 44, 45]. Optical systems that use spatial displacers or OAM may suffer from larger size, limited scalability, and stability issues, making it challenging to achieve long-time evolution of coin-position entanglement. Time-multiplexed optical systems can realize time-bin encoded quantum state by encoding position state in time domain. This configuration is scalable with respect to both the number of reachable steps and the accessible position Hilbert space, offering more flexibility in manipulating the walker's internal degree of freedom. Thus, maximal entangled states can be obtained by means of a fixed initial state and a specific coin operation[11, 12]. In addition, introducing dynamical disorder into the coin or shift operations in time-multiplexed optical systems can significantly enhance the coin-position entanglement and drive it towards maximal entanglement regardless of initial coin states[13–15]. However, the dynamical disorder also induces Anderson localization, which represents a fundamentally different mechanism from the NHSE. So far, there have been no reports on experimentally studying the influence of skin effect on the evolution of hybrid maximal entanglement dynamical in a non-Hermitian DTQWs system.

In this paper, we demonstrate the generation of maximal coin-position entanglement and the suppression of entanglement induced by the NHSE in a photonic DTQW system after a 20-step evolution. In particular, different types of DTQW scenarios are studied by changing the coin parameters, asymmetric loss efficiency, and initial states in a controlled way. The Lyapunov exponenet and von Neumann entropy under the different scenarios were numerically analyzed. Meanwhile, the polarization-resolved probability distributions and polarization-averaged growth rates after the 20-steps QWs were numerically and experimentally presented. Then, we chose specific coin parameters and asymmetric initial state to observed the evolution of entanglement and delocalization as the walk evolution steps. The results show that the choice of appropriate coin parameters and initial states can enhance entanglement after the 20-steps DTQWs. Further, we observed the phenomenon of suppression of evolution of hybrid maximal entanglement dynamical induced by the NHSE. We finally demonstrate that the suppression weakened with increasing coin parameters and enhanced with increasing asymmetric loss efficiency and evolution steps. The presented results provide a efficient way to study non-Hermitian properties on the evolution of entanglement in DTQWs systems.

II. THEORETICAL ANALYSIS

In a one-dimensional photonic DTQW, a photon (walker) moves left or right along a straight line based on a coin operation that manipulates its polarization. Taking the horizontal polarization state $|H\rangle = (1,0)^T$ and vertical polarization state $|V\rangle = (0,1)^T$ of the photon as walker's internal degree of freedom. The walker performs the spatial shift according to its internal state, and the resulting position is represented by the integer value $x \in Z$. Therefore, the coin-based QW own two separate spaces, namely coin space H_C and position space H_S. H_C is a two-dimensional Hilbert space spanned by $|H\rangle$ and $|V\rangle$. H_S is an infinite dimensional Hilbert space spanned by a set of orthogonal vectors $|x\rangle$.

The evolution operator of the DTQW can be defined by

$$\hat{U} = \hat{S}\left[\hat{L}(\gamma)\hat{C}(\theta) \otimes \hat{I}_p\right], \tag{1}$$

where $\hat{I}_p$ is the identity operator in space H_S. $\hat{C}(\theta)$ is the quantum coin operator in space H_C, which acts on the polarization of the photon using a half-wave plate (HWP). Its matrix representation is

$$\hat{C}(\theta) = \begin{pmatrix} \cos\theta & \sin\theta \\ \sin\theta & -\cos\theta \end{pmatrix}, \tag{2}$$

where θ is the rotation angle of the HWP relative to one of its optical axes. When the coin parameter θ is varied, it generates different superposition states of $|H\rangle$ and $|V\rangle$. Specifically, when $\theta = \pi/4$, the quantum walk becomes a Hadamard quantum walk.

In this one-dimensional photonic QW, we must account for system imperfections, such as depolarization effects, the efficiency ratio between the two polarizations, and the imperfect preparation of the initial state. Especially, optical components in the system, such as the coupling beam splitter, fiber delay loop, and waveplates, exhibit different losses for H-polarized and V-polarized photons, with the losses for V-polarized photons being slightly higher than those for H-polarized photons[40]. The polarization-dependent losses in the system can be described by a non-unitary loss operation $\hat{L}(\gamma)$, with matrix representation given by

$$\hat{L}(\gamma) = \sum_x |x\rangle\langle x| \otimes \left(|H\rangle\langle H| + e^{-\gamma}|V\rangle\langle V|\right) \tag{3}$$

Where γ is loss parameter indicating loss imbalance between the H-polarized and V-polarized photon. By changing the parameters γ and θ in a controlled way, we can generate a variety of DTQW scenarios. The shift operation $\hat{S}$ moves the photon's position x to $x+1$ if it is in the $|H\rangle$ state, or to $x-1$ if it is in the $|V\rangle$ state, which can be expressed as

$$\hat{S} = \sum_x |x-1\rangle\langle x| \otimes |V\rangle\langle V| + |x+1\rangle\langle x| \otimes |H\rangle\langle H| \tag{4}$$

Where $\hat{S}$ is implemented in the time domain using an optical feedback loop, where horizontally polarized photons travel along a longer path, while vertically polarized photons along a shorter path. The photon states from these two paths are coherently recombined at the output and fed back into the optical feedback loop for the next shift operation.

We consider that the initial photon state at $t = 0$ is a localized state at the original position $x = 0$, expressed as

$$|\psi_0(0)\rangle = |0\rangle \otimes [a_0(0)|H\rangle + b_0(0)|V\rangle], \qquad (5)$$

with the complex coefficients satisfying $|a_0(0)|^2 + |b_0(0)|^2 = 1$. The photon's wave function at the t-step evolution can be expressed as $|\psi_x(t)\rangle = \hat{U}^t|\psi_0(0)\rangle$. The system is a discrete-time simulation of non-unitary evolution driven by a non-Hermitian effective Hamiltonian $\hat{H}_{\text{eff}} = i\ln\hat{U}$. Thus, the normalized photon's wave function after t-steps evolves as[22–24, 46]:

$$\begin{aligned} |\psi_x(t)\rangle &= \frac{e^{-i\hat{H}_{\text{eff}}t}|\psi_0(0)\rangle}{\left\| e^{-i\hat{H}_{\text{eff}}t}|\psi_0(0)\rangle \right\|} \\ &= \sum_x |x\rangle \otimes [a_x(t)|H\rangle + b_x(t)|V\rangle] \end{aligned} \qquad (6)$$

with $x = -t, -t+2, \ldots, t-2, t$. The complex coefficients satisfy $\sum_x |a_x(t)|^2 + |b_x(t)|^2 = 1$ due to the normalized condition.

The characterization of $\hat{U}$ are reflected in the eigenstates and energy spectrum of $\hat{H}_{\text{eff}}$. The quantum walk governed by $\hat{U}$, which is influenced by the interplay of the effective coupling between polarization and position states, as well as polarization-dependent loss parameter. This interplay gives rise to the accumulation of eigenstates at the boundaries, a phenomenon known as the NHSE[22, 23]. Moreover, a major consequence of the NHSE is that the bulk bands of the system under open boundary conditions (OBC) differ significantly from those under periodic boundary conditions (PBC)[24]. When the system does not exhibit the NHSE, the energy spectrum under PBC consists of a set of open arcs. However, when the NHSE is present, the energy spectrum under PBC is formed by one or more closed loops enclosing a non-vanishing area. In contrast, under OBC, the energy spectrum consists of a set of open arcs located within the interior of the PBC loci.

The NHSE also influences bulk dynamics, leaving distinctive signatures in the Lyapunov exponent[23, 29, 47]. The long-time behavior of the Lyapunov exponent in bulk wave dynamics can generally reveal the presence of the non-Hermitian skin effect and is independent of the initial state. Here the Lyapunov exponent is defined as

$$\lambda(v) = \lim_{t\to\infty} \frac{\log|\langle x = vt|\psi_x(t)\rangle|}{t}, \qquad (7)$$

where v is the shift velocity. When the shift velocity v is set to 0, $\lambda(0)$ converges to a asymptotic value as t becomes large. The Lyapunov exponent $\lambda(0)$ describes the asymptotic growth rate of light intensity at $x = 0$, indicating the shifting behavior of the photon's wave function as it propagates through the lattice [29, 47]. When the asymptotic value is nonzero, the wave function exhibits unidirectional diffusion in the photonic lattice. In contrast, when the asymptotic value is zero, the wave packet exhibits unitary diffusion in the photonic lattice. In addition, the location of the peak of the Lyapunov exponent $\lambda(v)$ also shows how the wave function propagates along the lattice [23, 47]. Specifically, in the presence of NHSE, the peak of $\lambda(v)$ appear at finite shift velocity v, exhibiting a asymmetric profile at $v = 0$. While in the absence of NHSE, the peak of $\lambda(v = 0)$ appear at $v = 0$, which acquires a symmetric profile with respect to its peak at $v = 0$.

In the system, the initial state $|\psi_0(0)\rangle$ is pure, and after t-steps of non-unitary evolution with a small loss parameter γ, the state $|\psi_x(t)\rangle$ satisfies the normalization condition and can still be considered a pure state[48]. The coherent action of $\hat{S}$ and $\hat{C}$ leads to coin-position entanglement of the walker, which can be quantified through the von Neumann entropy[14, 15]. The von Neumann entropy is defined as $S_{\text{E}}(\rho_c) = -\text{Tr}(\rho_c\log_2\rho_c)$, where $\rho_c = \text{Tr}_{\text{p}}[|\psi_x(t)\rangle\langle\psi_x(t)|]$ is the reduced density matrix of coin state obtained by the partial trace over position. Combining Eq. (6), the reduced density matrix ρ_c is given by

$$\rho_c = \begin{pmatrix} \alpha(t) & \gamma(t) \\ \gamma^*(t) & \beta(t) \end{pmatrix}, \qquad (8)$$

with $\alpha(t) = \sum_x |a_x(t)|^2$, $\beta(t) = \sum_x |b_x(t)|^2$, $\gamma(t) = \sum_x a_x(t)b_x^*(t)$. Then the von Neumann entropy $S_{\text{E}}(\rho_c)$ is calculated by

$$S_{\text{E}}(\rho_c) = -\lambda_1\log_2\lambda_1 - \lambda_2\log_2\lambda_2, \qquad (9)$$

where λ_1 and λ_2 are the eigenvalues of matrix ρ_c expressed as

$$\lambda_{1,2} = \frac{1 \pm \sqrt{1 - 4\left[\alpha(t)\beta(t) - |\gamma(t)|^2\right]}}{2}, \qquad (10)$$

The walker state is separable when $S_{\text{E}} = 0$ and maximally entangled when $S_{\text{E}} = 1$. In addition to studying the entanglement properties of walker, the inverse participation ratio (IPR) can be used to quantify its localization (delocalization) properties[21, 49, 50]. It can be expressed as $\text{IPR}(t) = \left\{\sum_x [P_x(t)]^2\right\}^{-1}$, where $P_x(t) = |a_x(t)|^2 + |b_x(t)|^2$ represents the probability of finding the walker at site x at time t. When the photon's wave function $|\psi_x(t)\rangle$ is highly concentrated at certain positions x, the $P_x(t)$ increases, resulting in a smaller IPR value, which corresponds to a localized state. Conversely, if the photon's wave function $|\psi_x(t)\rangle$ is distributed across all positions, the IPR becomes larger, indicating a delocalized state. While the NHSE significantly influences
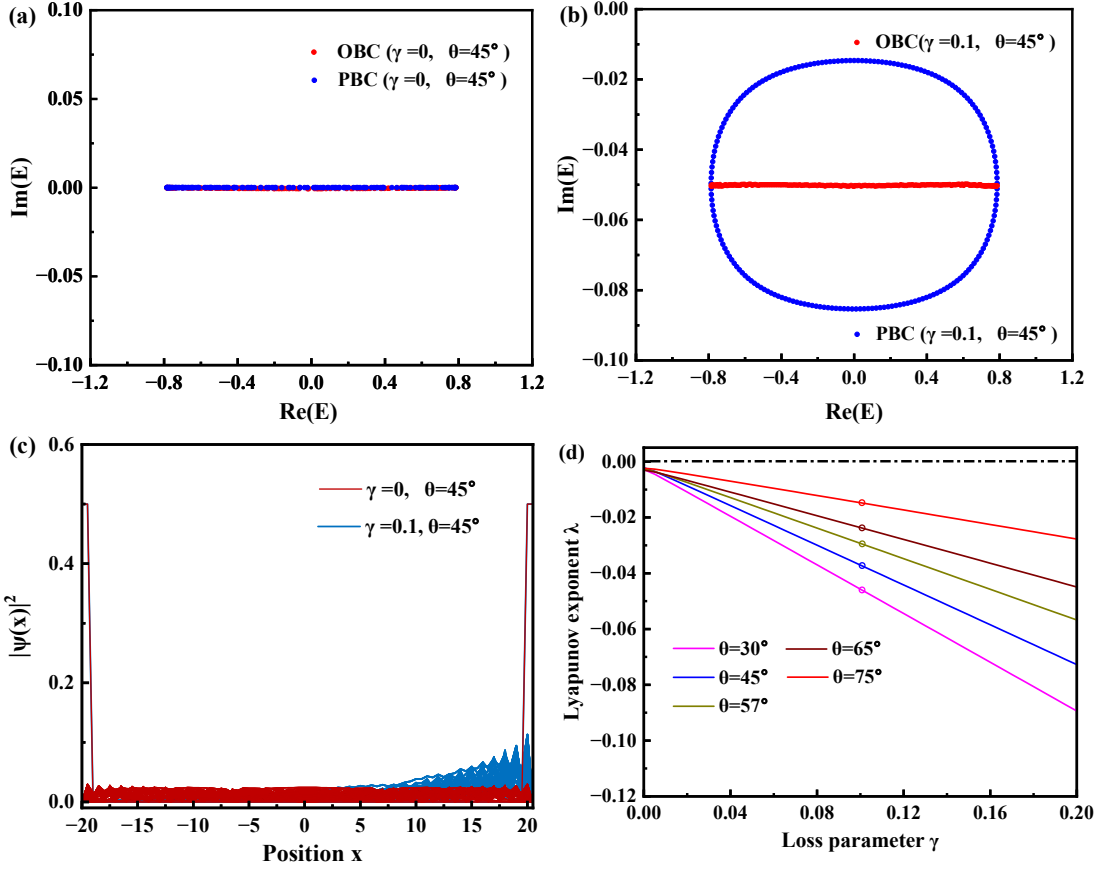
FIG. 1. (a) The eigen spectrums of the Hermitian DTQW for parameter values $\gamma = 0$, $\theta = 45$ under PBC and OBC. (b) The eigen spectrums of the non-Hermitian DTQW for parameter values $\gamma = 0.1$, $\theta = 45$ under PBC and OBC. (c) The spatial distribution of eigen wavefunctions in the system for different loss parameter γ at the coin operation parameter $\theta = 45$. (d) The Lyapunov exponent λ in the system as a function of the loss parameter γ for different coin operation parameter θ.

the walker's localization properties, here we focus on its impact on entanglement.

Fig. 1(a) and Fig. 1(b) shows the numerically calculated eigen spectrums of the Hermitian system for $\gamma = 0$, $\theta = 45°$ and the non-Hermitian system for $\gamma = 0.1$, $\theta = 45°$. The red dots represent the eigen spectrums under PBC, while the blue dots represent the eigen spectrums under OBC. It can be observed that when the loss parameter γ is set to 0.1, the energy spectrum for PBC forms closed loops and encloses a non-vanishing area, while energy spectrum for OBC forms a set of open arcs, indicating the presence of the NHSE. In the case of a non-zero loss parameter, the energy spectrum for PBCs exhibits similar closed loops. However, when $\gamma = 0$, the energy spectrum for PBC becomes a straight line, suggesting that the NHSE disappears as the loss parameter γ approaches zero. Fig. 1(c) shows the numerically calculated eigenstates of the Hermitian system for $\gamma = 0$, $\theta = 45°$ and the non-Hermitian system for $\gamma = 0.1$, $\theta = 45°$. The red and blue solid lines represent the eigen wavefunctions of the Hermitian system and the non-Hermitian system under OBC, respectively. It can be observed that the eigenstates of the Hermitian system are uniformly distributed in position space. When the loss parameter γ is detuned to 0.1, the eigenstates gradually localize at the boundaries, which is a characteristic feature of the NHSE. As the loss parameter γ is further increased, the eigenstates localize more rapidly at the boundaries (not shown in the Fig. 1(c)), exhibiting a more pronounced manifestation of the NHSE.

Fig. 1(d) shows the numerically calculated the lyapunov exponent λ of the system as a function of the loss parameter γ at different the coin operation parameter θ, using Eq. (7). Here, the coin operation parameter θ can be chosen as an arbitrary angle in the range $(0, \pi/2)$; for convenience, we select $\theta = 30°$ (pink line), $45°$ (blue line), $57°$ (yellow line), $65°$ (burgundy line), and $75°$ (red line), respectively. The walk steps t are set to 2000, at which point the $\lambda(0)$ converges to its asymptotic Lyapunov exponent λ. It can be observed that when $\gamma = 0$ (in this case, $\lambda(0)$ is approximately zero, and by increasing the number of steps, $\lambda(0)$ becomes closer to zero and converges to its asymptotic value, which can be considered zero), the amplitude of the Lyapunov exponent is zero for

all coin parameters, implying that no skin effects occur in the system. However, when $\gamma > 0$, the amplitude of the Lyapunov exponent become non-zero, implying that the skin effects occurs. Importantly, the amplitude of the Lyapunov exponent λ is gradually increasing with the increase of the loss parameter γ. Additionally, the amplitude of the Lyapunov exponent λ decreases as the increase of the coin parameter θ increases. This means that as the coin parameters increase further, the shift velocity of the wave function towards the boundary decreases, and the NHSE gradually weakens.
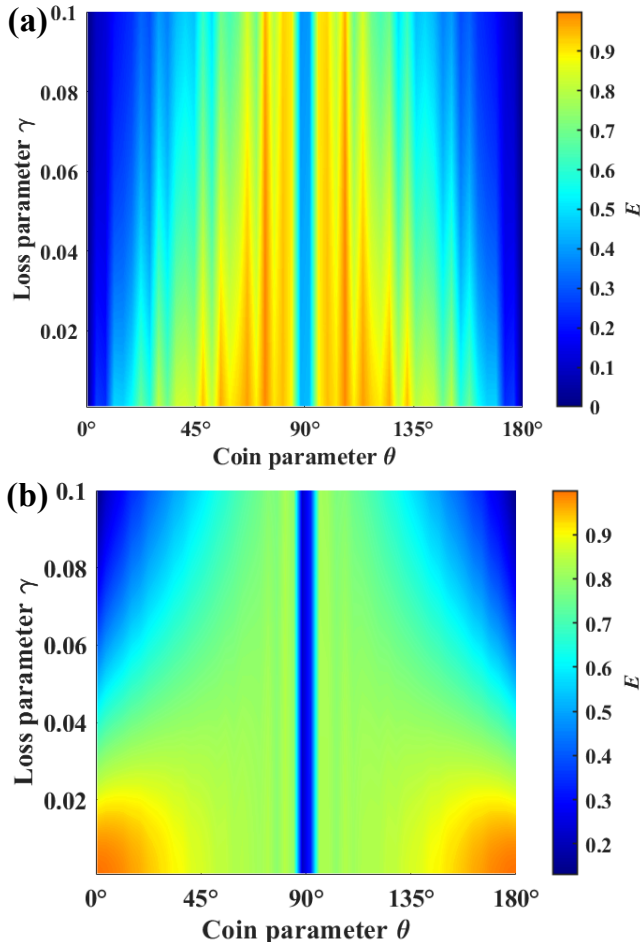

FIG. 2. The von Neumann entropy S_E of the coin-position entanglement as a function of the coin operation parameter θ and the loss parameter γ for the quantum walk with steps $t = 20$, considering different initial states. (a) The initial state is $|\psi_0(0)\rangle = |0\rangle \otimes |H\rangle$, where $a_0(0) = 1$ and $b_0(0) = 0$. (b) The initial state is $|\psi_0(0)\rangle = |0\rangle \otimes (|H\rangle + i|V\rangle)/\sqrt{2}$, where $a_0(0) = 1/\sqrt{2}$ and $b_0(0) = i/\sqrt{2}$.

For a fixed initial state, as walk steps increases, the coin-position entanglement approaches an asymptotic stable value. In general, this asymptotic value cannot reach its maximum in a Hadamard QW[11, 12]. Moreover, we know that the NHSE is not dependent on the specifics of the initial state. However this situation is corrupted in non-Hardamard DTQW systems. The coin-position entanglement in non-Hermitian DTQW systems also displays significantly different behaviors for different initial states. Fig. 2(a) shows numerically calculated the von Neumann entropy S_E of the walker for 20 steps as a function of the coin operation parameter θ and the loss parameter γ, with the initial state $|0\rangle \otimes |H\rangle$, using Eq. (9). Here, we consider the range of coin operation parameters θ to be $(0°, 90)$, and the loss parameter γ to be in the interval $(0, 0.1)$. When the coin parameters θ are chosen as 45°, 57°, and 65°, and the loss parameter γ is set to 0, the von Neumann entropy for 20 steps of the quantum walk is 0.8585, 0.982, and 0.996, respectively. Therefore, in non-Hadamard DTQW systems, the von Neumann entropy can be optimized to approach its maximum value when a specific small range of coin operation parameters is chosen. More interestingly, the von Neumann entropy S_E decreases slowly with the increase of the loss parameter. Furthermore, the larger the values of coin operation parameters, the slower the decrease in entanglement entropy. Therefore, combining with the results shown in Fig. 1(d), we can conclude that as the coin parameters increase further, the NHSE gradually weakens, and the decrease in entanglement entropy slows down. This also indicates that within these specific ranges of coin parameters, the system's entanglement properties can effectively resist the impact of the loss parameter.

Fig. 2(b) shows numerically calculated the von Neumann entropy S_E of the walker for 20 steps as a function of the coin parameter θ and the loss parameter γ, with the initial state $|0\rangle \otimes (|H\rangle + i|V\rangle)/\sqrt{2}$, using Eq. (9). When the coin parameter θ is gradually reduced from 45° to 0°, the von Neumann entropy increases continuously from 0.8753 to 1. Thus in non-Hadamard DTQW systems, the von Neumann entropy can be optimized to approach its maximum value when the coin operation parameter is chosen to be close to 0°. However, when the von Neumann entropy S_E of the coin-position entanglement exceeds 0.9, the range of the loss parameter γ and the coin operation parameter θ need to approximately bounded by $0 < \gamma < 0.02$ and $0 < \theta < 34.7°$. Combining the results shown in Fig. 1(d), we can conclude that as the coin parameters increase further, the NHSE is gradually enhanced, and the decrease of entanglement entropy is accelerating. This also indicates that within these specific ranges of coin parameters, the von Neumann entropy S_E of the coin-position entanglement changes rapidly with the loss parameter. With the theoretical analysis established, we now turn to the experimental setup and the analysis of the results.

III. EXPERIMENTAL DEMONSTRATIONS

The experimental setup of the one-dimensional photonic DTQWs is shown in Fig. 3. Our photon source is provided by a pulsed laser with a pulse width of 88 ps, a wavelength of 805 nm, and a repetition rate of 125 kHz.
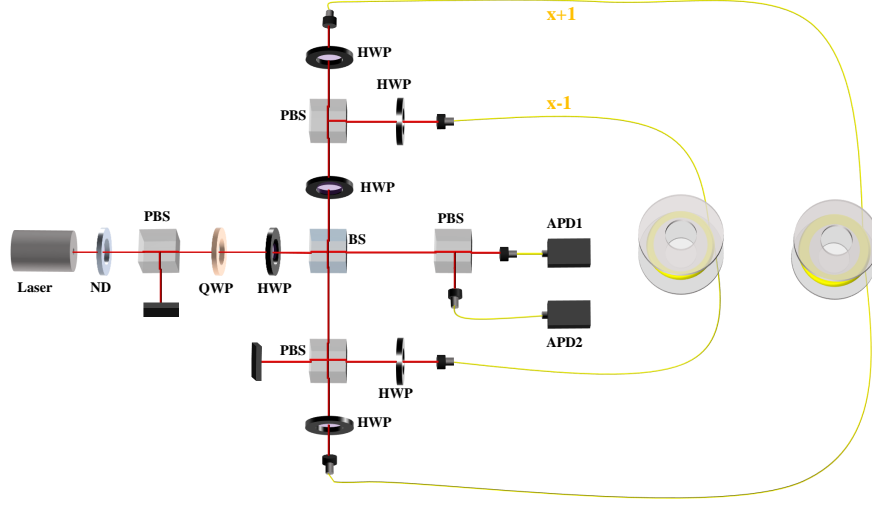
FIG. 3. Experimental setup of the one-dimensional photonic DTQW. HWP: half-wave plate; PBS:polarization beam splitter; QWP: quarter-wave plate; ND: neutral density filters; BS: 90/10 beam splitter; APD: single-photon detector; Setup dimensions: 1.5 m in free space and 31 m (30 m) in fiber.

The pulsed laser are attenuated to the single-photon level by using neutral density filters (ND). The initial state is prepared at position $|x = 0\rangle$ using standard HWP1 and QWP1. The quantum coin operation is implemented by another HWP2 to tune the coin parameter θ. The shift operation is implemented by the optical fiber feedback loop, which is composed of two polarization beam splitters (PBS1 and PBS2) and two optical fibers of different lengths. When photons pass through the PBS1, H-polarized photons enter the short fiber loop with a transmission time of 150 ns, while V-polarized photons enter the long fiber loop with a transmission time of 155 ns, which is 5 ns longer than that of a horizontally polarized photon. The resulting temporal difference of 5 ns between both polarization components corresponds to a step in the spatial domain of position $x+1$ or $x-1$. The two paths are coherently recombined by PBS2, and the photon is sent back to the input beam splitter PBS1 for the next step, such that the walker's position is mapped to the time domain.

In our experiment, the photon loss is caused by the experimental setup, and by measuring the transmission count rate in the long and short fiber loops, it is found that the loss of H-polarized photons per step is 3% less than that of V-polarized photons. Thus, the loss operation is implemented by HWPs introducing losses in short-path fibre channels. The probability that a photon will couple out of the fiber loop at each step of the walk is 59%. The characterization of the walker's wave function requires a series of experiments run consecutively, each of which produces at most a single click within a specific time window. These clicks are recorded by a computer through a time-to-digital converter interface. And with increasing numbers of walking steps, the loss of photons in this system increases and the probability of being de-

tected by the APD decreases. In order to determine the statistical distribution of walkers with a larger number of steps, hours of ensemble measurements are required. The influence of the external environment on the stability of the system, such as natural light pollution and wind disturbances, was reduced as much as possible.

After t steps of evolution, the photon wave packets are distributed in the $t + 1$ time windows corresponding with the positions $x = -t, -t + 2, \ldots, t - 2, t$. The two APDs are employed to measured the out-coupled photons's temporal and polarization properties, providing information about the number of time steps, as well as the spatial and coin states of the walker. We perform projection measurements on the polarization bases $|H\rangle$ and $|V\rangle$ for each time bin. The polarization-resolved position distribution probabilities are obtained by summing the counts of projection measurements onto the $|H\rangle$ and $|V\rangle$ states for each position, and then normalizing by dividing by the total sum of counts across all positions. As shown in Fig. 4, the polarization-resolved photon probability distributions for the 20-step quantum walk are present. Here, the initial state is choose as $|0\rangle \otimes |H\rangle$, and the coin parameters are selected as 45°, 57°, and 65°, respectively. It can be seen that these polarization-resolved photon position distributions clearly demonstrate the non-Gaussian behavior of the DTQW. Additionally, the experimental values of the von Neumann entropy for 20 steps are determined to be 0.842 ± 0.021, 0.968 ± 0.014, and 0.990 ± 0.010, respectively, by inserting these polarization-resolved photon probability distributions into equations (8), (9), and (10). These values are in good agreement with the numerical values. Therefore, using the initial state $|0\rangle \otimes |H\rangle$ at coin parameters $\theta = 65°$, our experiment generated the almost maximum coin-position entanglement in the 20-step quan-
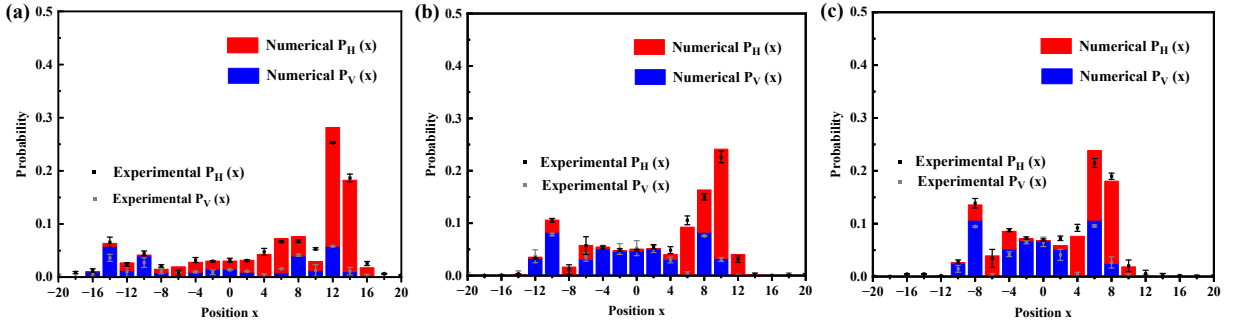
FIG. 4. (a)-(c) Experimental and numerical polarization-resolved probability distributions for the 20-step quantum walk with the initial state $|0\rangle \otimes |H\rangle$, at the coin operation parameter $\theta = 45°$ and loss parameter $\gamma = 0$. The red (top) and blue (bottom) bars are respectively the numerical results for the horizontal and vertical-polarization photon distributions. The gray dots represent the experimental measurements of the vertical-polarization-resolved photon distribution, while the black dots correspond to the experimental results for the sum of the polarization-resolved distributions. The error bars account for statistical uncertainties in photon number counting.
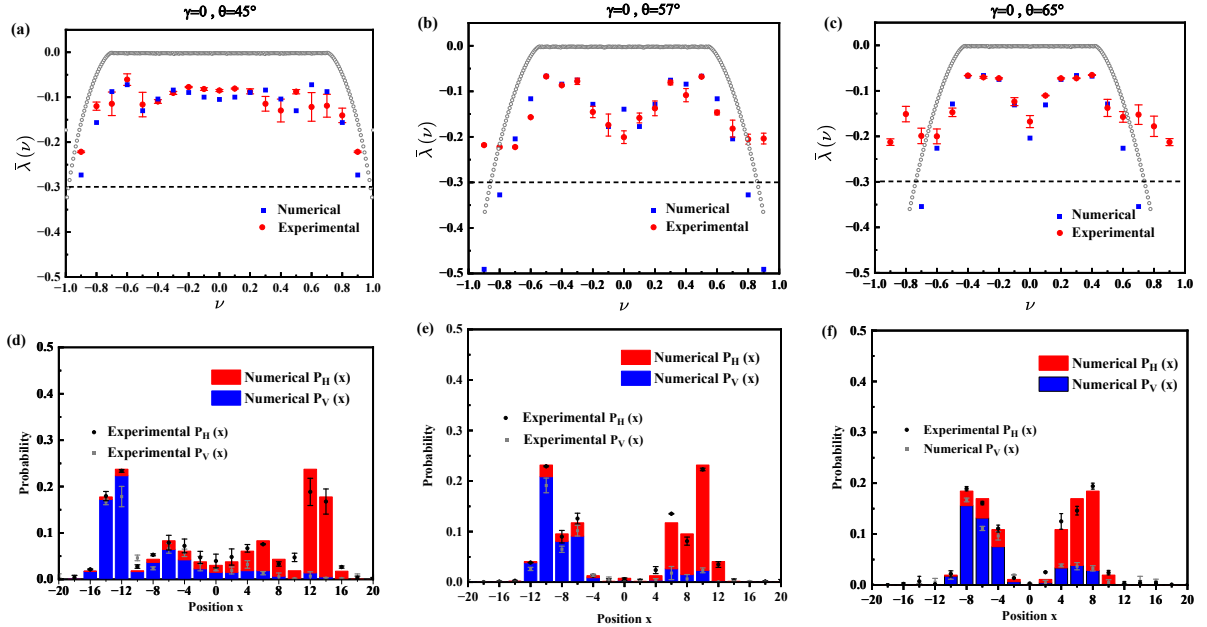

FIG. 5. (a)-(c) Experimental and numerical polarization-averaged growth rates $\bar{\lambda}(\nu)$ for the 20-step quantum walk with $\gamma = 0$ versus the shift velocity υ at $\theta = 45°$, $\theta = 57°$, and $\theta = 65°$. Red dots with error bars represents the experimental data and blue square correspond to numerical simulations. Black dashed lines indicate the threshold values below which experimental data are no longer reliable due to photon loss. (d)-(f) Experimental and numerical horizontally (vertically) polarized photon distribution for the 20-step quantum walk with the initial state $|0\rangle \otimes |H\rangle (|0\rangle \otimes |V\rangle)$, with $\gamma = 0$, versus the shift velocity υ at $\theta = 45°$, $\theta = 57°$, and $\theta = 65°$. The symbols in these figures are the same as those in Fig. 4.

tum walks. To compare the experimental and numerical distributions, we used the fidelity defined as $F = \sum_x \left(\sqrt{P_H^{\text{Exp}} P_H^{\text{Num}}} + \sqrt{P_V^{\text{Exp}} P_V^{\text{Num}}} \right)$, which ranges from 0 (complete mismatch) to 1 (identical distributions). The fidelities for the 20-step quantum walk are calculated as $F = 0.972 \pm 0.002$ at $\theta = 45°$, $F = 0.983 \pm 0.005$ at $\theta = 57°$, and $F = 0.977 \pm 0.003$ at $\theta = 65°$. Consequently, the non-Gaussian distribution of the quantum walk after 20 steps

of evolution confirms almost coherence in our experimental results.

To observe the NHSE, we measured the polarization-averaged growth rate $\bar{\lambda}(\upsilon) = \frac{1}{2}(\lambda_H(\upsilon) + \lambda_V(\upsilon))$ in our experiment. Here, $\bar{\lambda}(\upsilon)$ enables us to qualitatively capture the distinctive features of the Lyapunov exponent using the DTQW with 20 time steps. In Eq. (7), the polarization-resolved growth rates are defined
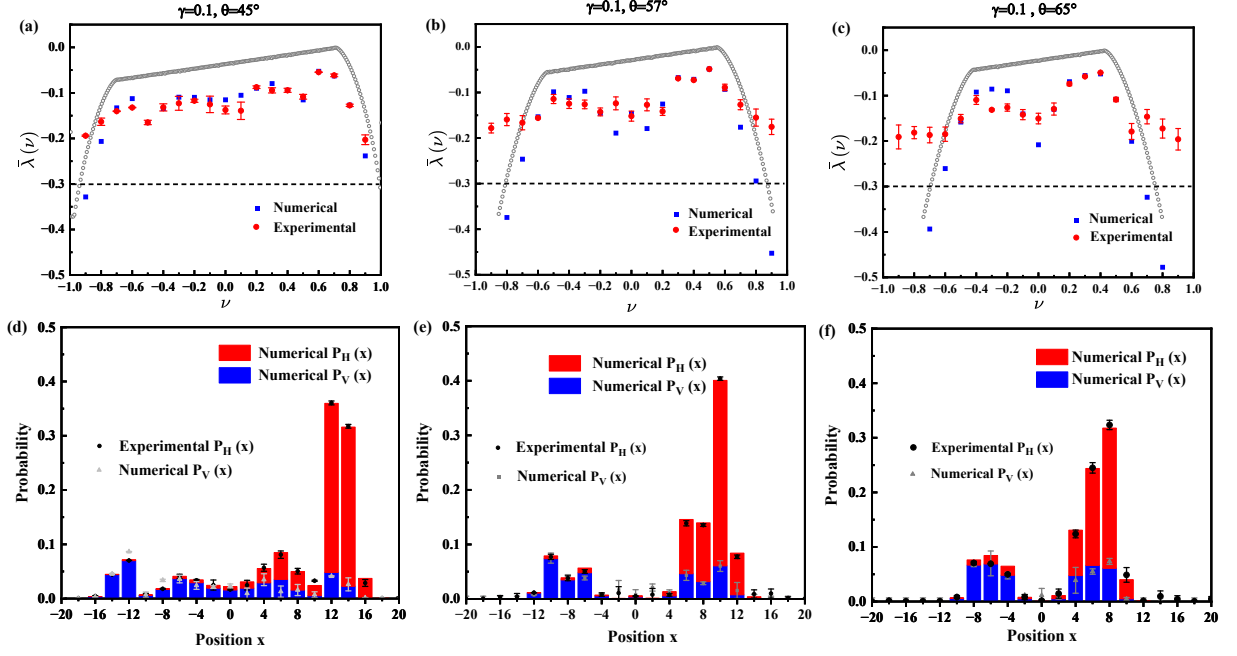
FIG. 6. (a)-(c) Experimental and numerical polarization-averaged growth rates $\bar{\lambda}(\nu)$ for the DTQW with $\gamma = 0.1$ versus the shift velocity υ at $\theta=45°$, $\theta=57°$, and $\theta=65°$. Red dots with error bars represents the experimental data and blue square correspond to numerical simulations. Gray circle are the numerical simulations results for the 2000-step quantum walk. (d)-(f) Experimental and numerical horizontally (vertically) polarized photon distribution for the 20-step quantum walk with the initial state $|0\rangle \otimes |H\rangle (|0\rangle \otimes |V\rangle)$, with $\gamma = 0.1$, versus the shift velocity υ at $\theta=45°$, $\theta=57°$, and $\theta=65°$. The symbols in these figures are the same as those in Fig. 4.

as $\lambda_{H(V)}(\upsilon) = \frac{1}{t} \log \left| \psi_x^{H(V)}(t) \right|$, where $\psi_x^{H(V)}(t) = \langle H(V) | \otimes \langle x | \psi_x(t) \rangle \otimes |H(V)\rangle$. To construct $\psi_x^{H(V)}(t)$, the initial state is chosen as $|0\rangle \otimes |H(V)\rangle$, and the probability distribution of photons in the coin state $|H(V)\rangle$ in the spatial mode $|x\rangle$ is measured projectively after the 20 walk steps. Fig. 5(a)-(c) show experimental and numerical polarization-averaged growth rates $\bar{\lambda}(\upsilon)$ for the 20-step quantum walk as functions of the shift velocity υ . Here, the loss parameter γ is chosen as 0, and the coin parameter θ is selected as 45°, 57° and 65°, respectively. Gray circle are the numerical simulations results for the 2000-step quantum walk, which is approximated as Lyapunov exponent of the system. From the gray circle and red data points, it can be seen that $\bar{\lambda}(\upsilon)$ with relatively small number of steps (t = 20) were able to characteristically capture the significant features of the Lyapunov exponent. Apparently, $\bar{\lambda}(\upsilon)$ shows a symmetric profile with respect to its peak at $\upsilon = 0$ and there is no non-Hermitian skinning effect. Such a profile directly originates from the directional propagation of probability in the bulk. As shown in Fig. 5(d)-(f), the horizontally (vertically) polarized photon distribution for the 20-step quantum walk with the initial state $|0\rangle \otimes |H\rangle (|0\rangle \otimes |V\rangle)$ are presented. The polarization-resolved photon distribution also exhibits a symmetric profile. The symmetric probability propagation naturally does not lead to the accumulation of population at the boundaries, but rather

to diffusion of population in the photonic lattice. Thus, we show that when the loss parameter $\gamma = 0$, there is no skin effect in the DTQW.

Fig.6(a)-(c) show also experimental and numerical polarization-averaged growth rates $\bar{\lambda}(\upsilon)$ for the 20-step quantum walk as functions of the shift velocity υ. Here, the loss parameter γ is chosen as 0.1, and the coin parameter θ is selected as 45°, 57° and 65°, respectively. From the gray circle and red data points, it can be also seen that $\bar{\lambda}(\upsilon)$ with 20 steps is able to qualitatively capture the significant features of the Lyapunov exponent. As shown in Fig. 6a, the maximum peak of $\bar{\lambda}(\upsilon)$ with the coin operation parameter θ =45° appeared at shift velocity $\upsilon = 0.6$; in Fig. 6b, the maximum peak with $\theta=57°$ appeared at $\upsilon = 0.5$; and in Fig. 6c, the maximum peak with $\theta=65°$ appeared at $\upsilon = 0.4$. Apparently, under the NHSE, $\bar{\lambda}(\upsilon)$ shows a asymmetric profile with respect to its peak at $\upsilon = 0$. Here, we demonstrated that when the loss parameter $\gamma = 0.1$, there is skin effect. In addition, the shift velocity υ corresponding to the maximum value of $\bar{\lambda}(\upsilon)$ is gradually moved towards the origin $\upsilon = 0$ with the increase of the coin parameter θ for the same loss parameter. Such profile directly originates from the directional propagation of probability in the bulk. As shown in Fig. 6(d-f), the horizontally (vertically) polarized photon distribution for the 20-step quantum walk with the initial state $|0\rangle \otimes |H\rangle (|0\rangle \otimes |V\rangle)$ are presented. The polarization-resolved photon distri-
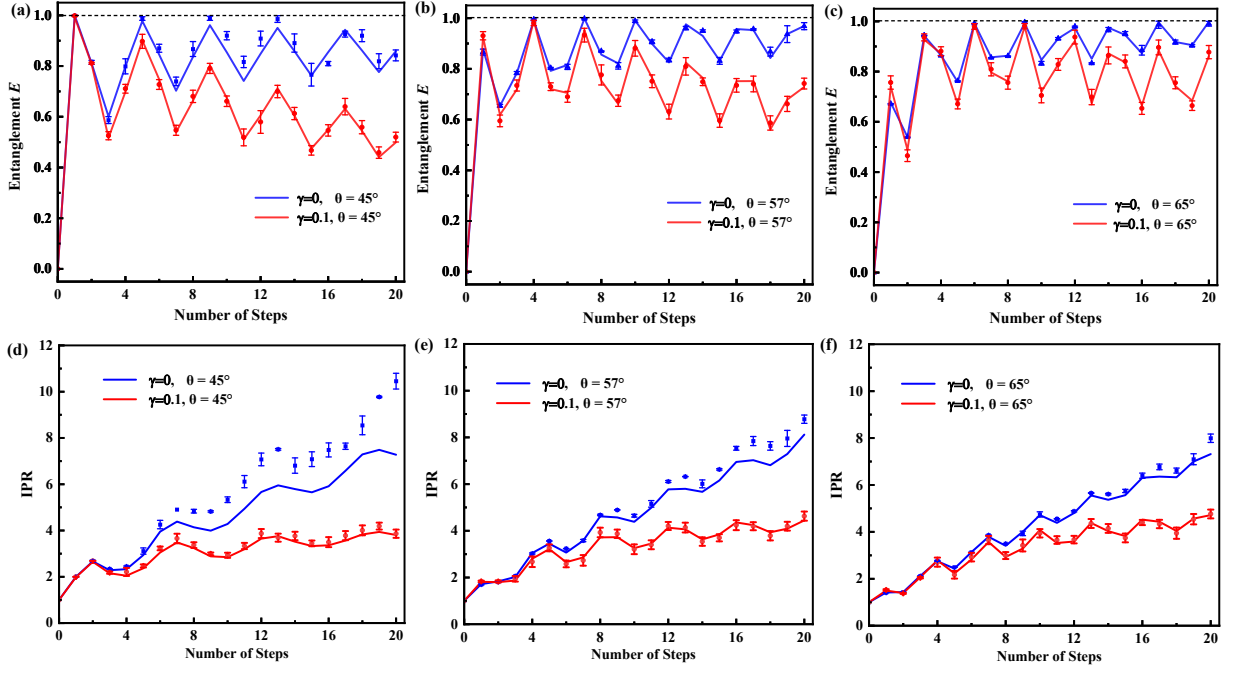
FIG. 7. (a)-(c) Experimental and numerical entanglement entropy S_E for the DTQW versus the evolution steps at $\theta=45°$, $\theta=57°$, and $\theta=65°$. (d)-(f) Experimental and numerical IPR for the DTQW versus the evolution steps at $\theta=45°$, $\theta=57°$, and $\theta=65°$. In Fig. 7, under the condition of $\gamma = 0$, the blue squares with error bars represent the experimental data, while the blue lines correspond to the numerical simulations. Similarly, under the condition of $\gamma = 0.1$, the red dots with error bars represent the experimental data, and the red lines correspond to the numerical simulations.

bution also exhibits a asymmetric profile. Where the maximum peak of photon distribution appeared at position $x = 12$ for $\theta = 45°$, at $x = 10$ for $\theta = 57°$, and at $x = 8$ for $\theta = 65°$. Since the localization of the population distribution is the unequivocal manifestation of the localization of bulk eigenstates by the NHSE. This means that, for a given loss parameter, increasing the coin parameter leads to a more uniform population distribution of photon across both sides, thereby weakening the skinning effect.

Fig. 7(a)-(c) shows experimental and numerical entanglement entropy S_E for the quantum walk as functions of the evolution steps. Here, the initial state is choose as $|0\rangle \otimes |H\rangle$, and the loss parameter γ are chosen as 0 and 0.1, respectively. The coin parameters are selected as 45°, 57°, and 65°, respectively. It can be observed that as the number of walking steps increases, the entanglement entropy of the quantum walk with loss parameter $\gamma = 0$ remains consistently higher than that of the quantum walk with loss parameter $\gamma = 0.1$, and this difference grows more significant as the number of steps increases. The results indicate that the suppression of entanglement in the non-Hermitian DTQW system ($\gamma = 0.1$) becomes more pronounced with the increasing number of walk steps. It is worth noting that the entanglement entropy S_E of the non-Hermitian DTQW system decays much more slowly as the number of steps increases when the operation parameter is $\theta = 65°$ compared to when the operation pa-

rameters are $\theta = 45°$ and $\theta = 57°$. As shown in Fig. 1(d), Fig. 2(a), and Fig. 6(a)-(c), these results further confirm that the suppression of entanglement, induced by NHSE, weakens as the coin parameters increase.

Note that entanglement suppression requires a large number of localized modes. As shown in Fig. 7(d)-(f), experimental and numerical IPR for the quantum walk as functions of the evolution steps are present. Here, the initial state is choose as $|0\rangle \otimes |H\rangle$, and the loss parameter γ are chosen as 0 and 0.1, respectively. The coin parameters are selected as 45°, 57°, and 65°, respectively. It can be observed that the IPR value of the quantum walk increases with the increase of the number of steps. Similar to the entanglement entropy characteristics observed in Fig. 7(a)-(c), the IPR of the quantum walk with loss parameter $\gamma = 0$ is also consistently higher than that of the quantum walk with loss parameter $\gamma = 0.1$. This difference becomes more pronounced as the number of walking steps increases. This is because, under the skin effect, the system soon reaches a nonequilibrium steady state in which population distribution of photon are localized at an boundaries, as shown in Fig. 6(d)-(f). As a result, the IPR of the non-Hermitian DTQW system decays more significantly with a larger number of evolution steps. Additionally, the IPR of the non-Hermitian DTQW system decays much more slowly as the number of steps increases when the operation parameter is $\theta = 65°$ compared to when the operation parameters are $\theta =$

$45°$ and $\theta = 57°$. Therefore, we show that the NHSE is able to suppress the coin-position entanglement as well as its delocalization in non-Hermitian DTQW systems, and that this suppression also decreases as coin parameters increases.

IV. CONCLUSION

In conclusion, we investigate the generation of maximal coin-position entanglement and the suppression of entanglement induced by NHSE in DTQWs. We provide a theoretical analysis of the Lyapunov exponent's dependence on both the loss parameter and the coin parameter. Our results show that the amplitude of the Lyapunov exponent increases with the loss parameter and decreases with the coin parameter, with a nonzero amplitude indicating the presence of skin effects. Additionally, we theoretically analyzed the dependence of the von Neumann entropy on the loss and coin parameters. We find that the von Neumann entropy can be optimized to approach its maximum value within specific ranges of coin operation parameters. It also increases with the loss parameter and decreases with the coin operation parameter.

Based on the theoretical analysis, we experimentally implemented a one-dimensional DTQW using a time-multiplexed fiber loop. We observed polarization-resolved photon probability distributions for a 20-step quantum walk. Our experiment demonstrated the generation of maximal coin-position entanglement in the 20-step quantum walk with specific coin parameters. Additionally, the polarization-averaged growth rate as a function of the shift velocity was experimentally measured. When the loss parameter is set to 0, the polarization-averaged growth rate and photon population distribution exhibit a symmetric profile, indicating the absence of the skin effect in the DTQW. However, when the loss parameter is set to 0.1, the polarization-averaged growth rate

shows an asymmetric profile and photon population are accumulated at the boundaries, indicating the presence of the skin effect. Importantly, the shift velocity corresponding to the maximum value of polarization-averaged growth rate is gradually moved towards the origin with the increase of the coin parameter for the same loss parameter. Therefore, we demonstrated that, for a given loss parameter, increasing the coin parameter leads to a more uniform photon population distribution across the photonic lattice, weakening the skin effect. We then studied the dynamic properties of entanglement and delocalization in DTQWs under different coin parameters. As the number of walking steps increases, we observed that the entanglement entropy and IPR of the quantum walk with a loss parameter of 0.1 gradually become lower than those of the quantum walk with a loss parameter of 0. Interestingly, for the same loss parameter, the entanglement entropy and IPR of the quantum walk decay much more slowly as the coin parameter increases. Therefore, our experiments also demonstrate that the suppression of entanglement in the non-Hermitian DTQW system becomes more pronounced with increasing evolution steps and weakens as the coin parameters increase. In the future, with the further development of photon quantum tomography technology, researchers will be able to experimentally reconstruct a more complete photon density matrix. This progress will enable our experimental platform to study complex quantum phenomena, including the detection of hybrid entanglement properties of multiple degrees of freedom in multi-particle systems, and the exploration of more challenging non-Hermitian open quantum systems.

---

[1] K. Pearson, Nature **72**, 342 (1905).

[2] Y. Aharonov, L. Davidovich, and N. Zagury, Phys. Rev. A **48**, 1687 (1993).

[3] A. M. Childs, Phys. Rev. Lett. **102**, 180501 (2009).

[4] A. M. Childs, D. Gosset, and Z. Webb, Science **339**, 791 (2013).

[5] M. S. Rudner and L. Levitov, Phys. Rev. Lett. **102**, 065703 (2009).

[6] S. Weidemann, M. Kremer, S. Longhi, and A. Szameit, Nature **601**, 354 (2022).

[7] N. Shenvi, J. Kempe, and K. B. Whaley, Phys. Rev. A **67**, 052307 (2003).

[8] V. Potoček, A. Gábris, T. Kiss, and I. Jex, Phys. Rev. A **79**, 012325 (2009).

[9] D. Qu, S. Marsh, K. Wang, L. Xiao, J. Wang, and P. Xue, Phys. Rev. Lett. **128**, 050501 (2022).

[10] X. Qiang, S. Ma, and H. Song, Intell. Comput. **3**, 0097 (2024).

[11] I. Carneiro, M. Loo, X. Xu, M. Girerd, V. Kendon, and P. L. Knight, New J. Phys. **7**, 156 (2005).

[12] G. Abal, R. Siri, A. Romanelli, and R. Donangelo, Phys. Rev. A **73**, 042302 (2006).

[13] S. J. Tao, Q. Q. Wang, Z. Chen, W. W. Pan, S. Yu, G. Chen, X. Y. Xu, Y. J. Han, C. F. Li, and G. C. Guo, Opt. Lett. **46**, 1868 (2021).

[14] R. Zhang, R. Yang, J. Guo, C. W. Sun, J. C. Duan, H. Zhou, Z. Xie, P. Xu, Y. X. Gong, and S. N. Zhu, Phys. Rev. A **105**, 042216 (2022).

[15] Q. Q. Wang, X. Y. Xu, W. W. Pan, K. Sun, J. S. Xu, G. Chen, Y. J. Han, C. F. Li, and G. C. Guo, Optica **5**, 1136 (2018).

[16] C. B. Naves, M. A. Pires, D. O. Soares Pinto, and

S. M. D. Queirós, Phys. Rev. A **106**, 042408 (2022).

[17] X. X. Fang, K. An, B. T. Zhang, B. C. Sanders, and H. Lu, Phys. Rev. A **107**, 012433 (2023).

[18] L. Xiao, T. Deng, K. Wang, Z. Wang, W. Yi, and P. Xue, Phys. Rev. Lett. **126**, 230402 (2021).

[19] L. Xiao, X. Zhan, Z. Bian, K. Wang, X. Zhang, X. Wang, J. Li, K. Mochizuki, D. Kim, N. Kawakami, *et al.*, Nat. Phys. **13**, 1117 (2017).

[20] K. Wang, X. Qiu, L. Xiao, X. Zhan, Z. Bian, W. Yi, and P. Xue, Phys. Rev. Lett. **122**, 020501 (2019).

[21] Q. Lin, T. Li, L. Xiao, K. Wang, W. Yi, and P. Xue, Phys. Rev. Lett. **129**, 113601 (2022).

[22] L. Xiao, T. Deng, K. Wang, G. Zhu, Z. Wang, W. Yi, and P. Xue, Nat. Phys. **16**, 761 (2020).

[23] Q. Lin, T. Li, L. Xiao, K. Wang, W. Yi, and P. Xue, Nat. Commun. **13**, 3229 (2022).

[24] K. Kawabata, T. Numasawa, and S. Ryu, Phys. Rev. X **13**, 021007 (2023).

[25] S. Weidemann, M. Kremer, T. Helbig, T. Hofmann, A. Stegmaier, M. Greiter, R. Thomale, and A. Szameit, Science **368**, 311 (2020).

[26] A. McDonald and A. A. Clerk, Nat. Commun. **11**, 5382 (2020).

[27] C. C. Wanjura, M. Brunelli, and A. Nunnenkamp, Nat. Commun. **11**, 3149 (2020).

[28] L. M. Chen, Y. Zhou, S. A. Chen, and P. Ye, Phys. Rev. B **105**, L121115 (2022).

[29] M. Gao, C. Sheng, Y. Zhao, R. He, L. Lu, W. Chen, K. Ding, S. Zhu, and H. Liu, Phys. Rev. B **110**, 094308 (2024).

[30] E. Flurin, V. V. Ramasesh, S. Hacohen Gourgy, L. S. Martin, N. Y. Yao, and I. Siddiqi, Phys. Rev. X **7**, 031023 (2017).

[31] V. V. Ramasesh, E. Flurin, M. Rudner, I. Siddiqi, and N. Y. Yao, Phys. Rev. Lett. **118**, 130501 (2017).

[32] C. A. Ryan, M. Laforest, J. C. Boileau, and R. Laflamme, Phys. Rev. A **72**, 062317 (2005).

[33] M. Karski, L. Förster, J.-M. Choi, A. Steffen, W. Alt, D. Meschede, and A. Widera, Science **325**, 174 (2009).

[34] H. Schmitz, R. Matjeschk, C. Schneider, J. Glueckert, M. Enderlein, T. Huber, and T. Schaetz, Phys. Rev. Lett. **103**, 090504 (2009).

[35] F. Zähringer, G. Kirchmair, R. Gerritsma, E. Solano, R. Blatt, and C. F. Roos, Phys. Rev. Lett. **104**, 100503 (2010).

[36] L. Sansoni, F. Sciarrino, G. Vallone, P. Mataloni, A. Crespi, R. Ramponi, and R. Osellame, Phys. Rev. Lett. **108**, 010502 (2012).

[37] A. Crespi, R. Osellame, R. Ramponi, V. Giovannetti, R. Fazio, L. Sansoni, F. De Nicola, F. Sciarrino, and P. Mataloni, Nat. Photonics **7**, 322 (2013).

[38] S. K. Goyal, F. S. Roux, A. Forbes, and T. Konrad, Phys. Rev. Lett. **110**, 263602 (2013).

[39] T. Giordani, E. Polino, S. Emiliani, A. Suprano, L. Innocenti, H. Majury, L. Marrucci, M. Paternostro, A. Ferraro, N. Spagnolo, *et al.*, Phys. Rev. Lett. **122**, 020503 (2019).

[40] A. Schreiber, K. N. Cassemiro, V. Potoček, A. Gábris, P. J. Mosley, E. Andersson, I. Jex, and C. Silberhorn, Phys. Rev. Lett. **104**, 050502 (2010).

[41] A. Schreiber, K. Cassemiro, V. Potoček, A. Gábris, I. Jex, and C. Silberhorn, Phys. Rev. Lett. **106**, 180403 (2011).

[42] A. Schreiber, A. Gábris, P. P. Rohde, K. Laiho, M. Štefaňák, V. Potoček, C. Hamilton, I. Jex, and C. Silberhorn, Science **336**, 55 (2012).

[43] Q. Lin, W. Yi, and P. Xue, Nat. Commun. **14**, 6283 (2023).

[44] P. Xue, R. Zhang, H. Qin, X. Zhan, Z. Bian, J. Li, and B. C. Sanders, Phys. Rev. Lett. **114**, 140502 (2015).

[45] X. Zhan, L. Xiao, Z. Bian, K. Wang, X. Qiu, B. C. Sanders, W. Yi, and P. Xue, Phys. Rev. Lett. **119**, 130501 (2017).

[46] S. Longhi, Phys. Rev. B **108**, 075121 (2023).

[47] S. Longhi, Phys. Rev. Res. **1**, 023013 (2019).

[48] H. P. Breuer and F. Petruccione, *The theory of open quantum systems* (Oxford University Press, USA, 2002).

[49] J. Ghosh, Phys. Rev. A **89**, 022309 (2014).

[50] A. Buarque and W. d. S. Dias, Phys. Rev. E **100**, 032106 (2019).